Resistivity imaging over porphyry copper systems in the Red Mountain district, southwest Colorado, USA

Eric Anderson[1], Maryla Desczc-Pan[1], Doug Yager[1], Kyle Eastman[2], Bennett Hoogenboom[1]
[1]U.S. Geological Survey, Denver, Colorado, USA
[2]Montana Bureau of Mines and Geology, Butte, Montana, USA

Abstract. The Red Mountain district in southwestern Colorado produced base and precious metals hosted in breccia pipes and vein structures related to an extensive lithocap that overlies pervasive quartz-sericite-pyrite alteration. A helicopter-borne time-domain electromagnetic survey flown over the district yielded resistivity values that range from tens to thousand or more ohm-m, with lesser resistivity values in the lithocap and greater resistivity values in the rocks with propylitic alteration. A 60 m-thick, low resistivity zone subparallel to topography characterizes the magmatic-hydrothermal breccia pipes. A broad zone of low resistivity that may envelope epithermal deposits spans multiple flight lines and occurs beneath rocks with argillic alteration. A 50 m-thick low resistivity zone occurs beneath quartz-sericite-pyrite alteration and may indicate porphyry deposit at depth.

1 Introduction

The Red Mountain district is located along the structural margin of the Silverton caldera in southwest Colorado (Figure 1). Past production includes precious (Au, Ag) and base metals (Pb, Zn, Cu) hosted in breccia pipes and vein structures (Gonzales and Larson 2017). The district provides a unique opportunity to image the subsurface of porphyry copper systems because extensive erosion in rugged topography has exposed nearly a kilometer of crust from the mountain peaks to the valley floors. Surface alteration assemblages have been mapped using a combination of field mapping with X-ray diffraction analysis and imaging spectroscopy (Bove et al. 2007; Dalton et al. 2007), which provide a detailed understanding of surface mineralogy.

In this contribution, we build upon previous geophysical investigations of the Silverton caldera (Anderson et al. 2023) and focus on the lithocap in the Red Mountain district that is underlain by pervasive quartz-sericite-pyrite alteration. Airborne time-domain electromagnetic data are used to show the distribution of conductive material from the surface to depths around 300 m. We present resistivity inversion results along select flight lines that traverse outcropping components of the lithocap and underlying quartz-sericite-pyrite alteration and integrate these results into a three-dimensional modelling environment to discuss the implications for exploration.

2 Geologic setting

The Red Mountain district along the Silverton caldera margin is composed predominantly of Paleogene volcano-plutonic rocks that intrude and overlie variably metamorphosed sedimentary, volcanic, and intrusive rocks of Precambrian age and relatively undeformed sedimentary rocks of Paleozoic and Mesozoic age (Figure 1: Burbank and Luedke 1964; Yager and Bove 2007). The caldera margin consists of zones of concentric and radial faults and fractures. The flat-lying volcanic rocks include lava flows and related volcaniclastic rocks ranging in composition from andesite to rhyolite (Yager and Bove 2007) and have thickness around 850 m inside the caldera (Luedke and Burbank 2000).

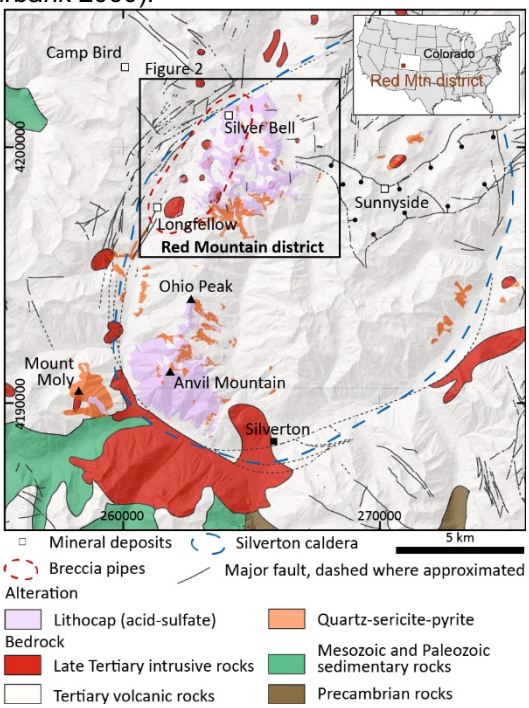

Figure 1. Generalized geologic map of the Silverton caldera in southwest Colorado. The Red Mountain district is along the caldera margin and consists of pervasively altered Tertiary volcanic and lesser intrusive rocks. Modified from Casadevall and Ohmoto (1977).

In the Red Mountains, an extensive lithocap formed around 23 Ma (Figure 2: Bove et al. 2001). The lithocap includes silicified rock surrounded by argillic alteration, and additional areas mapped as variations of quartz-alunite-pyrophyllite (Bove et al. 2007). Rocks having pervasive quartz-sericite-pyrite alteration crop out in the valleys below. Propylitic alteration assemblages and local areas of vein-related quartz-sericite-pyrite occur outward of the lithocap. Drill hole observations show that with increasing depth the alteration changes from advanced argillic to argillic to phyllic to weakly propylitic to strongly potassic at depths around 800 to 1200 m (Gilzean 1984). Magmatic-hydrothermal

breccia pipes formed along a north-northeast trending zone that is 2 km-wide extending from the Longfellow to Silver Bell mines (Gonzales and Larson 2017). The pipes have diameter around 150 m and are known to extend to depths of 300 m. The deposits have a high-sulfidation mineral assemblage that includes dickite, alunite, and pyrophyllite with enargite and pyrite. In addition, polymetallic veins occur in caldera-related structures. Ferricrete deposits that mark the emergence of paleowater tables are common east of the Red Mountains in the valley floors.

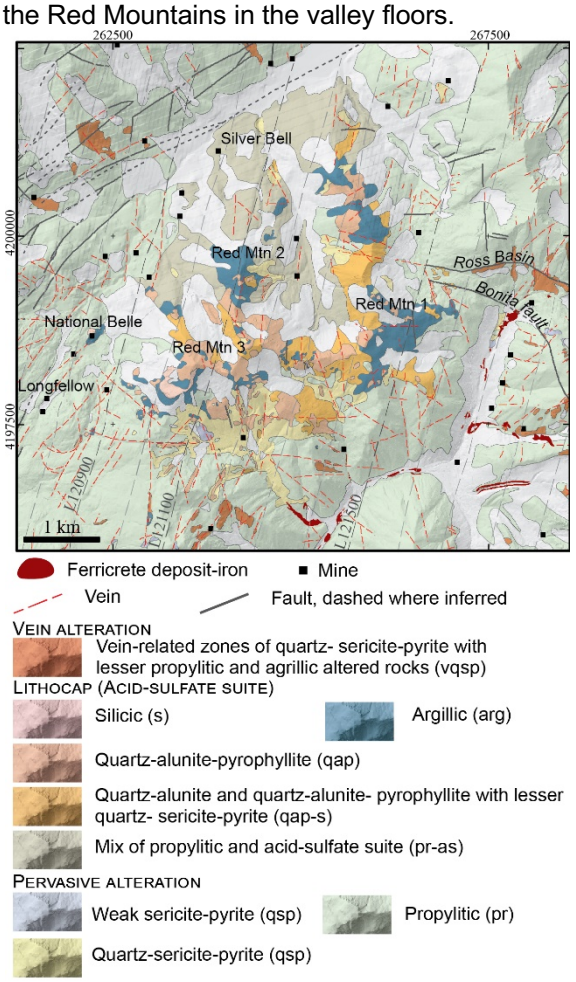

Figure 2. Alteration map of the Red Mountain district (modified from Bove et al. 2007). Dashed grey lines are flight lines with labelled lines shown in Figure 4.

3 Methodology

A helicopter-borne time-domain electromagnetic survey was flown by Geotech Ltd. over the Silverton caldera in 2019 (Hoogenboom et al., 2022). These data were subset to the Red Mountains district and had parallel flight lines oriented north-northeast with 600 m spacing and nominal terrane clearance for the transmitter-receiver loop of 110 m. Data were collected in 54-time channels ranging from 4.63 to 8254 µsec. A tau map, which measures the inductive response of a conductive target, was used for qualitative interpretation. Tau spans the measured time range and is dependent on conductance, not response magnitude, and, therefore, the presence of a good conductor is amplified and emphasized independently of its depth.

The time-domain electromagnetic data were inverted (Hoogenboom et al. 2022) along survey profile lines using the method described by Auken et al (2015). The 1D inversions used a 30-layer model with a 500 m maximum depth allowing for significant variations in depth of investigation beneath resistive and conductive areas. The inversion result is sensitive to sensor-to-source distance and may therefore be less resolved when sensor height is too large. The results were gridded with cell size of 5 m and provide a 2D quantitative estimate of the resistivity changes from the surface to around 300 m depth.

4 Results

The Tau map shows lateral changes in areas that exhibit good conductance, or low resistivity (Figure 3). The zone of magmatic-hydrothermal breccia deposits shows low resistivity along the entire length from Longfellow to Silver Bell mine where the bedrock is altered to propylitic and a mix of acid-sulfate assemblages. Low resistivity is also mapped on Red Mountain 1 and westward to Red Mountain 3 where the bedrock is variably altered to silicic, quartz-alunite-pyrophyllite, and lesser quartz-sericite-pyrite assemblages. North and south of Red Mountain 1 are rocks with propylitic assemblages that exhibit relatively high resistivity.

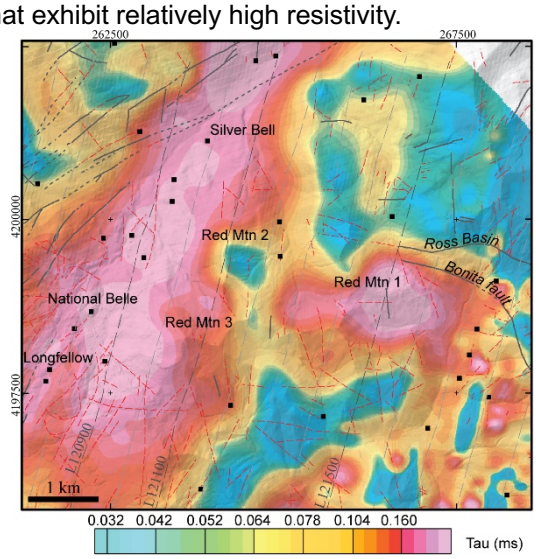

Figure 3. Contour map of Tau showing a qualitative distribution of resistivity changes with warm and cool colours indicating low and high resistivity, respectively.

The inverted resistivity sections provide estimates of how resistivity varies with depth beneath the flight lines (Figure 4). The sections extend approximately 7 km over pervasively altered rock. Line L120900 over the breccia deposits and rocks with propylitic alteration exhibits a prominent zone of low resistivity at 50 m depth with thickness around 60 m and is subparallel to topography (Figure 4a). The zone deepens and thickens to the north near the structural margin of the caldera. Line L121100 traverses the lithocap over Red Mountains

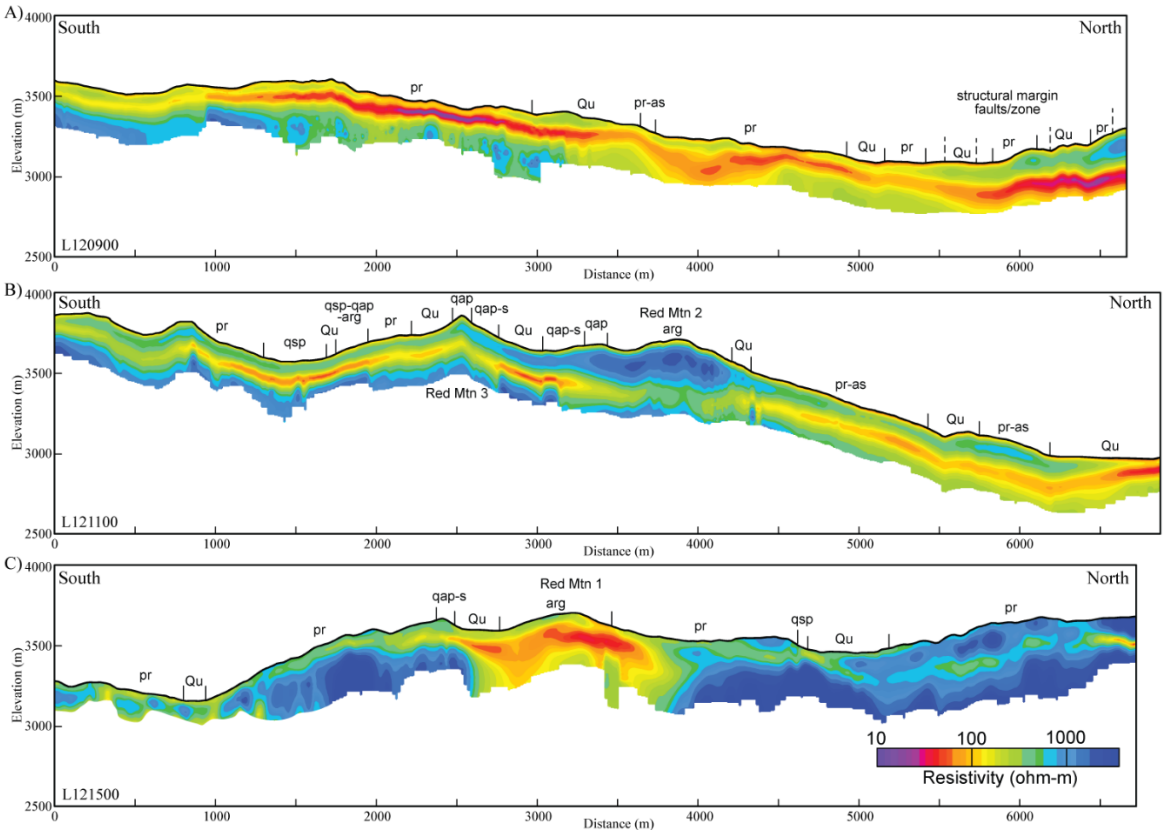

Figure 4. *Resistivity sections for flight lines A) L120900, B) L121100, and C) L121500. Mapped surface alteration extent indicated with abbreviations and vertical lines. Abbreviations: arg=argillic, pr=propylitic, pr-as=mix of propylitic and acid-sulfate suite, qap=mix of quartz-alunite and quartz-alunite-pyrophyllite, qap-s=quartz-alunite and quartz-alunite-pyrophyllite with lesser quartz-sericite-pyrite, qsp=quartz-sericite-pyrite stockwork veins, Qu=Quaternary deposit. See Figure 2 for flight line location.*

2 and 3 (Figure 4b). A zone of low resistivity subparallel to topography occurs on the south and north flanks of Red Mountain 3. The argillic alteration mapped on Red Mountain 2 has high resistivity and a zone of low resistivity parallels topography along the northern flank where the surface alteration consists of mixed propylitic and acid-sulfate assemblages. Line L121500 shows a zone of low resistivity on Red Mountain 1 where the rocks have argillic alteration assemblages, and high resistivity to the north and south (Figure 4c).

5 Discussion and implications

The Red Mountain district exhibits outcropping alteration patterns that show silicified ridges underlain by argillic and quartz-alunite-pyrophyllite alteration with quartz-sericite-pyrite assemblages at lower elevations. The lithocap formed at 23 Ma and has variable resistivity (Figure 5). Supergene processes commonly occur in the weathering environment of porphyry copper systems (Sillitoe 2005) and the formation of clay minerals and groundwaters with high dissolved solids can reduce subsurface resistivity (Dentith and Mudge 2014). Anderson et al. (2023) used reported drill hole observations of oxidized minerals to attribute low resistivity zones subparallel to topography in areas of pervasively altered rocks on Mount Moly, Anvil Mountain, and Ohio Peak (Figure 1) to supergene processes. In addition, ferricrete deposits are spatially distributed downslope from areas of intense alteration (Verplank et al. 2007; Yager and Bove 2007) and an indication that such processes have occurred.

The north-northeast-trending zone of breccia deposits from Longfellow to Silver Bell exhibits a prominent low resistivity response in the Tau map (Figure 3). In this area, the inverted resistivity sections show a blanket-like low resistivity zone (Figures 4,5). The highly fractured rocks in the pipes and along the structural margin of the caldera are permeable areas for paleo- and present-day groundwater to oxidize sulfides to depths near the top of the low resistivity zone. The flight line spacing (600 m) is likely too wide to image individual pipes that have diameters around 150 m. Thus, the Tau map provides a reconnaissance tool when exploring for breccia pipes and the inversions provide estimate to the depth at which enrichment may be expected.

At higher elevations in the Red Mountains, a broad area of low resistivity is imaged from the surface to depths around 300 m in adjacent flight lines (Figure 5). The Tau map indicates low resistivity on Red Mountain 1 that continues eastward to Red Mountain 3, and high resistivity on Red Mountain 2 (Figure 3). Argillic alteration assemblages are mapped on Red Mountains 2 and 3, yet the inverted resistivity sections show that these areas are underlain by high and low resistivity, respectively. Argillic alteration is clay rich and

characterized by the presence of dickite and trace to 40% fine-grained quartz, along with varying amounts of pyrite (Bove et al. 2007). The discrepancy in subsurface resistivity may be due to quartz content where an increase in quartz would increase resistivity. The low resistivity zone on Red Mountain 1, is therefore, likely due to the presence of clay, and the weathering of pyrite may have produced acidic conditions favorable for supergene processes. The area is surrounded by rocks having propylitic alteration and high resistivity. Thus, the low resistivity zone may contain epithermal deposits.

On the north and south flanks of Red Mountain 3, a thin low resistivity zone parallels the topography (Figures 4,5). This area is underlain by quartz-sericite-pyrite assemblages, most notably to the south (Figure 2). The veinlets associated with such alteration may have provided the necessary permeability and source metals for supergene processes. The geometry of the lithocap overlying rocks having quartz-sericite-pyrite assemblage is suggestive of porphyry deposit at depth. Thus, a thin low resistivity zone beneath mapped quartz-sericite-pyrite assemblages may be a good indicator of underlying porphyry-style mineralization.

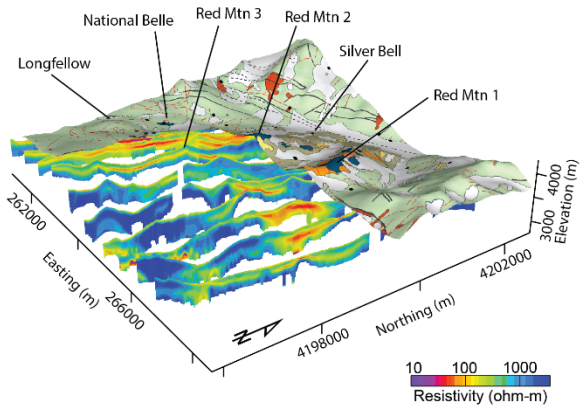

Figure 5. Three-dimensional perspective view of the Red Mountain district showing alteration patterns mapped at the surface and resistivity sections at depth.

Acknowledgements

We thank the U.S. Forest Service (USFS) and the Mineral Resources Program of the U.S. Geological Survey (USGS) for funding the airborne time-domain survey. Jean Legault and the Geotech team are thanked for data acquisition and thoughtful discussions. Any use of trade, firm, or product names is for descriptive purposes only and does not imply endorsement by the U.S. government.

References

Anderson ED, Yager DB, Deszcz-Pan M, Hoogenboom BE, Rodriguez BD, Smith BD (2023) Geophysical data provide three dimensional insights into porphyry copper systems in the Silverton caldera, Colorado, USA. Ore Geology Reviews 152:105223. https://doi.org/10.1016/j.oregeorev.2022.105223

Auken E, Christiansen AV, Kirkegaard C, Fiandaca G, Schamper C, Behroozmand AA, Binley A, Nielsen E, Effersø F, Christensen NB, Sørensen K, Foged N, Vignoli G (2015) An overview of a highly versatile forward and stable inverse algorithm for airborne, ground-based and borehole electromagnetic and electric data. Exploration Geophysics 46:223-235

Bove DJ, Hon K, Budding KE, Slack JF, Snee LW, Yeoman RA (2001) Geochronology and geology of late Oligocene through Miocene volcanism and mineralization in the western San Juan Mountains, Colorado. US Geological Survey Professional Paper 1642, 30 p. http://doi.org/10.3133/pp1642

Bove DJ, Yager DB, Mast MA, Dalton JB (2007) Alteration map showing major faults and veins and associated water-quality signatures of the Animas River watershed headwaters near Silverton, southwest Colorado. US Geological Survey Scientific Investigations Map 2976, 18-p. pamphlet, 1 plate, scale 1:24,000

Burbank WS, Luedke RG (1964) Geology of the Ironton quadrangle, Colorado, Geologic Quadrangle: US Geological Survey Geologic Quadrangle Map GQ-291, scale 1:24,000. http://doi.org/10.3133/gq291

Casadevall T, Ohmoto H (1977) Sunnyside Mine, Eureka mining district, San Juan County, Colorado; geochemistry of gold and base metal ore deposition in a volcanic environment. Econ. Geol. 72:1285-1320

Dalton JB, Bove DJ, Mladinich CS, Rockwell BW (2007) Imaging spectroscopy applied to the Animas River watershed and Silverton caldera. US Geological Survey Professional Paper 1651, Ch. E2, 141-159

Dentith M, Mudge ST (2014) Geophysics for the mineral exploration geoscientist. Cambridge University Press, Cambridge, United Kingdom

Gilzean MN (1984) The Nature of the Deep Hydrothermal System, Red Mountain District, Silverton, Colorado. Dissertation, University of California

Gonzales DA, Larson RA (2017) An overview of the mineral deposits of the Red Mountain mining district, San Juan Mountains, Colorado. In Karlstrom KE, Gonzales DA, Zimmerer MJ, Heizler M, Ulmer-Scholle DS (eds) The Geology of the Ouray-Silverton Area, New Mexico Geological Society 68th Annual Fall Field Conference Guidebook 133-140.

Hoogenboom BE, Deszcz-Pan M, Anderson ED, Rodriguez BD, Smith BD, Yager DB (2022) Airborne electromagnetic and magnetic survey data, Silverton, Colorado, 2019. US Geological Survey data release, https://doi.org/10.5066/P92IADBP

Luedke RG, Burbank WS (2000) Geologic map of the Silverton and Howardsville quadrangles, southwestern Colorado. US Geological Survey Geologic Investigation Series Map I–2681, scale 1:24,000. http://doi.org/10.3133/i2681

Sillitoe RH (2005) Supergene oxidized and enriched porphyry copper and related deposits. Economic Geology 100th Anniversary Volume 29:723-768

Verplank PL, Yager DB, Church SE, Stanton MR (2007) Ferricrete classification, morphology, distribution, and carbon-14 age constraints. In Church SE, von Guerard P, Finger SE (eds) Integrated investigations of environmental effects of historical mining in the Animas River watershed, San Juan County, Colorado, US Geological Survey Professional Paper 1651, 723–744

Yager DB, Bove DJ (2007) Geologic framework. In Church SE, von Guerard P, Finger SE (eds) Integrated investigations of environmental effects of historical mining in the Animas River watershed, San Juan County, Colorado, US Geological Survey Professional Paper 1651, 107–140

Multi-scale and multi-source hyperspectral imaging for mapping lithium-bearing minerals

René Booysen[1,2], Moritz Kirsch[1], Samuel T. Thiele[1], Sandra Lorenz[1], Yuleika Madriz[1], Paul A. M. Nex[2], Judith Kinnaird[2], Richard Gloaguen[1]
[1]Helmholtz Institute Freiberg for Resource Technology, Helmholtz-Zentrum Dresden-Rossendorf, Germany
[2]School of Geosciences, University of the Witwatersrand, South Africa

Abstract. The transition towards a net-zero economy has led to an increased need for several critical raw materials required for green technologies. Lithium (Li) is one of these materials. Significant mineral exploration using sustainable, efficient and innovative methods is required to not only improve mineral detection and mapping, but also to foster social acceptability for the mining and exploration industry. Hyperspectral imaging (HSI) allows for fast and systematic identification of key minerals. In this contribution, we propose an innovative approach for exploration by using hyperspectral data from multiple sensors at various scales to non-invasively map ore and pathfinder minerals. We showcase this approach in an open-pit and under-ground sites in South Africa, Namibia and Germany by acquiring data in the short-wave infrared (SWIR) with both a tripod and a drone. Hand-samples and drill-cores were used to identify the relevant minerals as well as for training/validation purposes. Using computer vision techniques, we were able to create a three-dimensional (3D) point cloud of the sites with HSI attributes to allow for the subsequent spectral mapping of relevant Li-bearing minerals. Results were validated using drill-core data, LIBS measurements and geochemical analyses of hand samples.

1 Introduction

The transition towards a green economy has led to a rise in demand for certain raw materials. Among these materials, Lithium (Li) stands out, as it is increasingly used in green technologies such as in rechargeable batteries for electric vehicles (Herrington 2021). Recycling alone cannot sustain this increased demand, which has reignited the focus on primary raw materials. Conventional exploration methods are typically involve laborious fieldwork, supported by geophysical surveying, which can prove to be costly, time-consuming, and often encounter low social acceptance of mining and exploration activities. Thus, a renewed approach to mineral identification and exploration is required.

We propose to use hyperspectral imaging (HSI) as a non-invasive method for the sustainable exploration and mapping of Li-bearing minerals. HSI is a method whereby a single image is acquired at hundreds of different wavelengths of the electromagnetic spectrum. Each pixel of the resulting data cube contains spectral information that can ultimately be used to identify mineral types (Shippert 2003). HSI allows us to acquire data safely from a distance as some targets might not be easily accessible. Furthermore, it allows for fast and systematic identification of key minerals and can provide information about mineral abundances and associations.

In recent years, the use of HSI for identifying and mapping minerals directly in the field has set particular emphasis on satellite and plane-based platforms (Van der Meer et al. 2012). We suggest using an innovative approach where hyperspectral data is acquired from both drone-borne and ground-based platforms at various scales (from open-pit and underground outcrops to drill-cores) to map ore pathfinder minerals for the targeting of Li.

To demonstrate our approach, we acquired data in the visible and near-infrared (VNIR) as well as short-wave infrared (SWIR) range of the electromagnetic spectrum at various Li-bearing deposits in South Africa, Namibia and Germany. In South Africa we acquired data from various pegmatite outcrops containing Li. One such example is from the Noumas 1 pegmatite body that contains spodumene and lepidolite (Figure 1). In Namibia, we acquired data from the main open-pit at the Uis tin mine. The LCT pegmatite hosts Li-bearing minerals such as cookeite and petalite amongst others (Booysen et al. 2022). In Germany, we acquired data from the historic underground Zinnwald mine, which is a Sn-W-Li greisen-type deposit and contains the Li-bearing mineral zinnwaldite (Kirsch et al. 2023, *in review*).

By using computer vision techniques, we created hyperclouds of the targeted outcrops, i.e., three-dimensional (3D) point cloud that are attributed with the full hyperspectral information (Thiele et al. 2021). This allowed us to map the relevant mineralization directly on the within the context of the outcrop geometry and easily integrate information from hand-samples and drill-cores (where possible) to identify relevant minerals as well as for training and validation purposes. This approach enables rapid and efficient mapping of complex terrains in a sustainable exploration scheme, and can be used for monitoring and optimisation of ore extraction.

Figure 1. Large green spodumene crystals found at the Noumas 1 pegmatite body in South Africa. The spodumene is surrounded by large white feldspar crystals.

2 Methodology and results

Due to emerging development of sensor technology towards small and robust solutions, hyperspectral sensors have become available for geological fieldwork. Not only can hyperspectral SWIR sensors be used on tripods in the field, but can now be deployed on civilian unmanned aerial vehicles (UAVs; also known as drones). This has allowed more flexible data acquisitions of targets at a relatively high spectral and spatial resolution.

For ground-based hyperspectral data acquisition, we used a tripod mounted Specim AisaFENIX that acquires data in the VNIR and SWIR range of the electromagnetic spectrum (400 nm – 2500 nm). A generator and a work-station are required in order to capture data in the field (Figure 2. a). For underground acquisition, adequate artificial lighting was required in addition. For UAV-based data acquisition we used a HySpex Mjolnir VS-620. The Mjolnir also acquires data in the VNIR and SWIR range (400 nm – 2500 nm). The UAV that we used is a custom-built octocopter, with the entire system, including the sensor and gimbal, weighing below 20 kg (Figure 2. b).

3D models of the various outcrops were produced through Structure-from-Motion, Multi-View-Stereo (SfM-MVS) photogrammetry. The RGB photos were captured in the field with a Sony camera, and were used for the SFM-MVS workflow in Agisoft Metashape. The 3D models were used to properly correct the hyperspectral data in the python-based toolbox *Hylite* (Thiele et al. 2021). The hyperspectral data is back-projected on the 3D model and transformed to a so-called hypercloud. The attributes of the 3D model allow us to correct for varying illumination conditions. Ultimately, by transforming the hyperspectral image into a hypercloud, we create a 3D pointcloud containing x, y and z coordinates as well as hyperspectral reflectance attributes.

Figure 2. a The tripod mounted AisaFENIX sensor in the field with a workstation consisting of a computer and generator. **b** The HySpex Mjolnir attached to the gimbal and mounted to a custom-built octocopter.

Hand samples and drill-cores were used to identify the minerals present at each outcrop. The samples were analysed in the laboratory with LWIR (long-wave infrared) and SWIR sensors. Spectra extracted from the data were compared to spectral libraries (the USGS and CSIRO spectral libraries) to identify the minerals in the samples. This allowed us to identify Li-bearing minerals such as lepidolite found at Noumas 1 (Figure 3), and other path finder minerals. We used these extracted spectra to create spectral libraries specific to each outcrop. With this information, we used machine learning algorithms (such as supervised classifications), minimum wavelength mapping and band ratios to map the relevant minerals directly on the hypercloud. In Figure 4 we show one such example where Li-bearing minerals were mapped in 3D at the main open-pit at the Uis mine. The results were validated using spectral point measurements, in-situ LIBS measurements and geochemical analyses such as XRF and XRD.

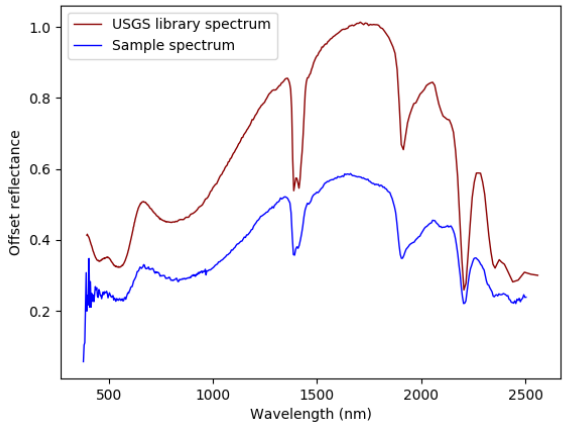

Figure 3. Spectrum of lepidolite taken from hyperspectral SWIR data of a hand sample (in blue) compared with a lepidolite spectrum taken from the USGS spectral library (in red).

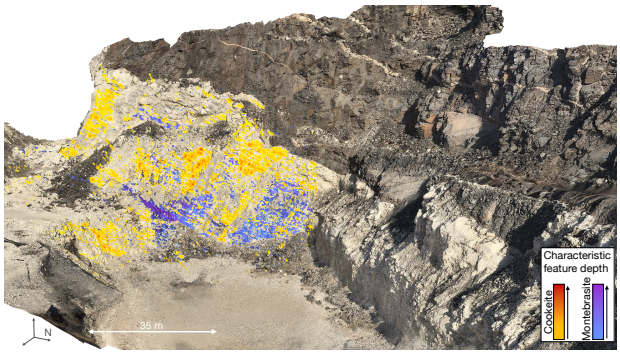

Figure 4. 3D model of the main open-pit at the Uis tin mine. Mapped Li-bearing minerals are shown in yellow and blue. Cookeite is shown in yellow and red, with red indicating a higher abundance of cookeite. Montebrasite is shown in blue and purple, with purple indicating a higher abundance (Booysen et al. 2022).

3 Discussion

In this contribution, we demonstrate the use of hyperspectral data from both UAV and tripod platforms for the exploration of open-pit and underground Li-hosting deposits. There are many unique challenges that accompany the acquisition of hyperspectral data on both tripod and drone platforms. For tripod data acquisition, a stable and good vantage point is required to capture optimal data of the targeted body, however, finding such a vantage point is not always possible. This is where UAV-based platforms can be useful. On the other hand, data acquired from a drone requires more complex corrections due to the platform's continuous movement during acquisition. Although the usage of both platforms has their own challenges to overcome, the fact that we have both options available allow us to use the most appropriate platform for each situation.

Proper data corrections are imperative for the successful use of the data. More conventional remote sensing methods such as satellite- and plane-based HSI have widely accepted and standardized correction steps. However, the correction procedure of data acquired with ground-based and drone-borne platforms are still considered novel. With this demonstration, we show a robust workflow with our advanced python-based toolbox, Hylite. Hylite corrects for various effects such as different incident angles and ambient light. Thiele et al. 2021).

By acquiring hyperspectral data of the hand samples and drill-cores first, we can not only identify and map the Li-bearing minerals directly, but also identify mineral associations. This aids us in directing focus to certain alterations that may be associated with mineralization. Furthermore, by creating a hypercloud we transform a normal hyperspectral image into a 3D data set with each point containing its own spectrum, latitude, longitude and elevation. This allows us to produce a geometrically correct and spatially continuous mineral map. By producing a 3D mineral map, geologists can improve their sampling strategy for further investigations. This approach is also meant to supplement geological fieldwork by providing a qualitative discrimination of geological domains in order to rapidly direct mining or exploration activities. It may be possible to selectively mine specific areas within the deposit based on this kind of data. The same approach can be used to map key mineralization in underground mines with the addition of artificial lighting (Kirsch et al. 2023, *in review)*.

Taking a hyperspectral multi-source approach has allowed us to acquire geological information rapidly and efficiently, allowing us to save time and keep costs down compared to conventional methods. Additionally, by using innovative and non-invasive methods during mining and exploration activities we can foster a higher degree of social acceptance in the mining and exploration industry.

4 Conclusion and outlook

Our study demonstrates the potential of a multi-source hyperspectral approach in generating mineral maps that are both geometrically accurate and spatially continuous. This approach has proven to be a valuable asset for the exploration and optimised extraction of critical raw materials such as Li, despite certain limitations. Notably, HSI promotes more socially acceptable methods for mining and exploration by using innovative and non-destructive methods. The next step would be to incorporate the time component, and with repeated acquisitions and real-time processing, we can provide 4D models that allow the monitor of the evolution of a geological target.

Acknowledgements

We would like to acknowledge Andrada Mining for their valuable support during the field campaign and data acquisition at the Uis tin mine. Additionally,

we would like to thank the South African Council of Geosciences for their assistance and support during fieldwork in South Africa. We would also like to acknowledge the Zinnwald visitors mine in Germany for their support during our hyperspectral campaign at the mine. This work received funding from HIF, the DSI-NRF Centre of Excellence; CIMERA as well as the European Regional Development Fund and the Land of Saxony.

References

Herrington, R., (2021) Mining our green future. *Nature Reviews Materials*, 6(6), 456-458. https://doi.org/10.1038/s41578-021-00325-9

Shippert, P., (2003). Introduction to hyperspectral image analysis. *Online Journal of Space Communication*, 2(3), 8.https://ohioopen.library.ohio.edu/spacejournal/vol2/iss3/8

Van der Meer, F. D., Van der Werff, H. M., Van Ruitenbeek, F. J., et al., (2012) Multi-and hyperspectral geologic remote sensing: A review. *International Journal of Applied Earth Observation and Geoinformation*, 14(1), 112-128. https://doi.org/10.1016/j.jag.2011.08.002

Booysen, R., Lorenz, S., Thiele, S. T., et al., (2022) Accurate hyperspectral imaging of mineralised outcrops: An example from lithium-bearing pegmatites at Uis, Namibia. *Remote Sensing of Environment*, 269, 112790. https://doi.org/10.1016/j.rse.2021.112790

Kirsch, M., Mavroudi, M., Thiele, S. T., et al., (2023) Underground hyperspectral outcrop scanning for automated mine-face mapping — the Lithium deposit of Zinnwald/Cínovec. *Photogrametric Record.* Under review

Thiele, S. T., Lorenz, S., Kirsch, M., et al. (2021) Multi-scale, multi-sensor data integration for automated 3-D geological mapping. *Ore Geology Reviews*, 136, 104252. https://doi.org/10.1016/j.oregeorev.2021.104252

Remote sensing and radiometric data for the detection of hydrothermal alteration zones with mineral potential at Yarra Wurta cliff, Australia

Juan E. Mosquera R.[1]
[1]*Geology department, National University of Colombia, Bogotá, Colombia*

Abstract. This study aimed to investigate the mineralization potential of the Yarra Wurta Cliff area, located approximately 45 km northeast of the Olympic Dam deposit in Australia, using spectral analysis and interpretation of geophysical data. This research used an integrated approach combining Landsat and ASTER satellite imagery, along with radiometry data provided by the Australian government, to detect and map hydrothermal disturbance in a study area in Australia. The results showed a good correlation between the radiometry data and the distribution of hydrothermal alteration, especially iron, copper and gold alteration. Although certain rocks showed clear signs of hydrothermal alteration, it is unclear whether they are more susceptible to alteration or whether other factors, such as their proximity to the source of the hydrothermal fluids, play a more important role. Overall, these findings
findings suggest that hydrothermal alteration in the Yarra Wurta Cliff area may be of interest for prospecting for minerals of economic interest.

1 Introduction

In mineral resource exploration, the detection of hydrothermal alterations is a key tool for identifying potential mineral deposits. Remote sensing is an important tool for the detection of these alterations over large areas, as it provides an aerial perspective and wide coverage. In this work, information from two remote sensors, Landsat and ASTER, was used to detect and characterize hydrothermal alterations in the Yarra Wurta cliff area in South Australia (Figure 1-2).

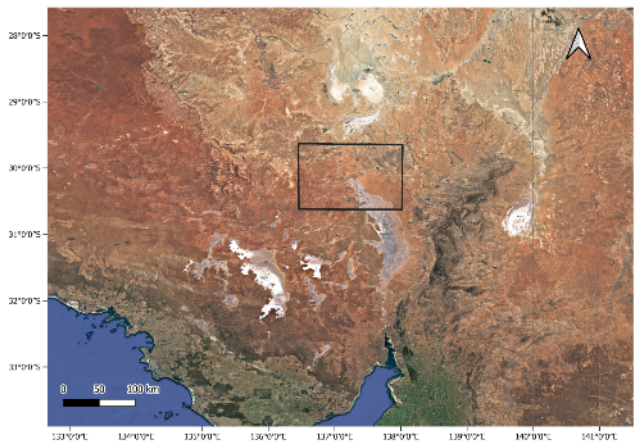

Figure 1. Location of the study zone, located in South Australia. Basemap: Google Hybrid, Map data ©2023 Google.

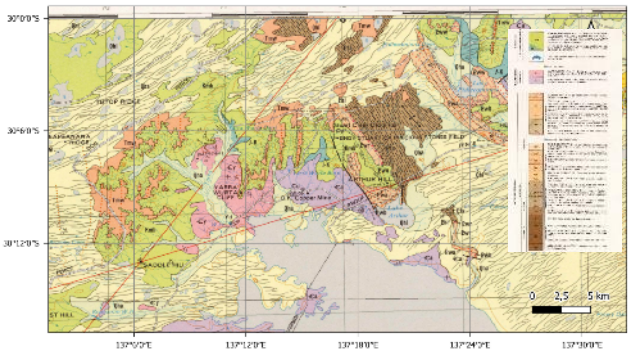

Figure 2. Geological map 1:250000 of Andamooka, the area is smaller than figure 1. Adapted from Raymond, O.L. (2002)

In addition to the remote sensing information, radiometric data were also used to corroborate the information and determine if the alterations were related to areas with anomalies in radioactive elements.

The methodology used to detect and characterize the hydrothermal alterations in the Yarra Wurta cliff area is presented and the results obtained are discussed.

2 Materials and methods

2.1 multi-sensor data

For this study, Was used Landsat-8/OLI data scenes LC09_L2SP_099081_20230217_20230220_02_T1 .The processing level corresponds to collection 2, level 2.

In addition, ASTER L1T satellite scenes, (AST_L1T_00303242001011242_20150415081131_13760),(AST_L1T_00303242001011250_20150415081132_61472) were used.

Landsat 9-OLI and ASTER data used in this study were acquired from the USGS Earth Explorer program.

No geometric, atmospheric, or radiometric corrections were applied to the Landsat 9-OLI and ASTER images, as both images were already rectified.

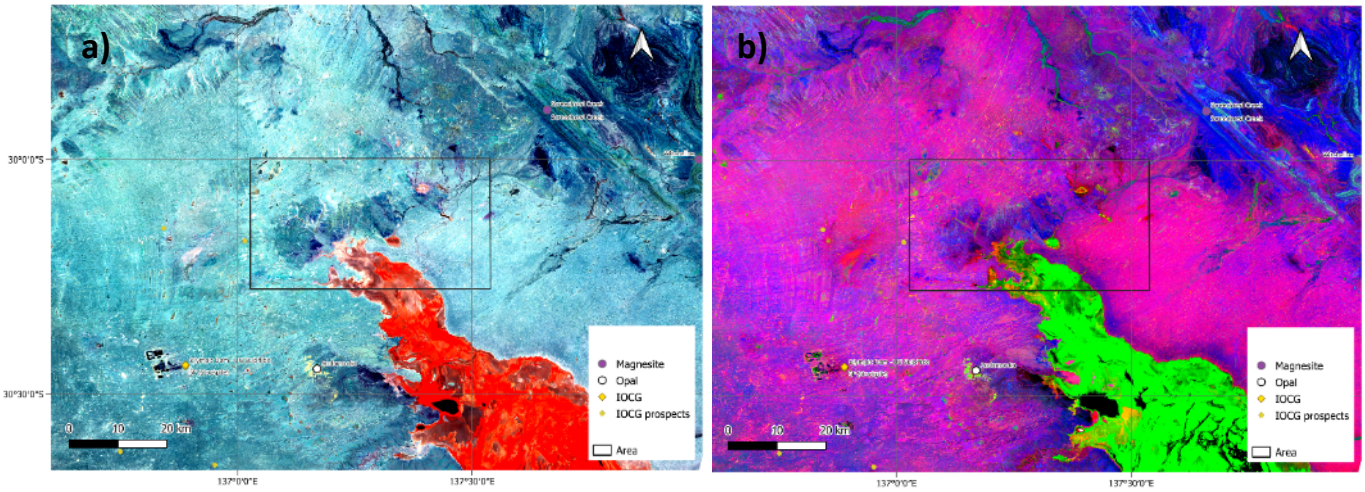

Figure 3. Landsat colour composites and band ratios: (a) RGB bands (5,6,7) dark blue represents hydrothermally altered rocks, (b) RGB bands (4/2,6/7,6/5) Blue represents altered rocks.

2.2 Colour composite

Colour composite is a technique used in remote sensing and image processing to combine three or more separate monochrome images into a single image.

Each monochrome image is typically derived from a different spectral band, with each band capturing different characteristics of the scene or object being imaged. By combining these bands into a single colour image, the resulting image provides more information and can be easier to interpret.

Colour composites are often used to highlight specific mineralogy and lithology in rocks, allowing geologists to more easily identify and characterize geological features. Githenya, L.et al. (2019)

2.3 Band ratio

Band ratios are a technique used to enhance specific features in satellite imagery by combining two or more spectral bands. In remote sensing, certain combinations of spectral bands can provide unique information about the earth's surface.

Band ratios are calculated by dividing the digital number (DN) values of one spectral band by the DN values of another spectral band. The resulting ratio values can then be displayed as a new image, with areas of interest highlighted based on the chosen spectral bands. The choice of spectral bands for band ratios depends on the application and the specific features of interest. The resulting images can be further processed using techniques such as false colour composites or image classification to extract information about the earth's surface.

2.4 Supervised classification

Supervised classification is a widely used technique in remote sensing for land cover mapping. In this study, we used supervised classification to identify different land cover classes in the study area.

The plugin SCP in Qgis was used to perform the classification, a set of training samples was selected for each land cover class based on visual interpretation of high-resolution satellite imagery and ground truth data.

2.5 Radiometric Data

Gamma-ray spectrometry-geophysics is a method used to determine the levels of potassium (K), uranium (eU), and thorium (eTh) on the surface of the Earth.

Radiometry data were obtained from the Geoscience Australia portal, identified as GSSA Andamooka percent Potassium grid geodetic, GSSA Andamooka ppm Thorium grid geodetic and GSSA Andamooka pmm Uranium grid geodetic. These data were used to provide information on the geology, including the identification of hydrothermal altered zones.

3 Results

3.1 Colour Composite

A colour compositing technique was used to generate a composite RGB (red, green, blue) image to highlight areas of hydrothermal disturbance. The combination of bands used was 5 (near infrared), 6 (shortwave infrared) and 7 (mid-infrared) .(Figure 3a).

This combination of bands allows obtaining a composite image in which hydrothermal alterations are highlighted (Figure 3a). According to Githenya, L.et al. (2019), this technique is widely used for the detection of hydrothermal alterations in mining areas and has proven to be effective in the identification of alteration minerals and the characterization of rocks at surface.

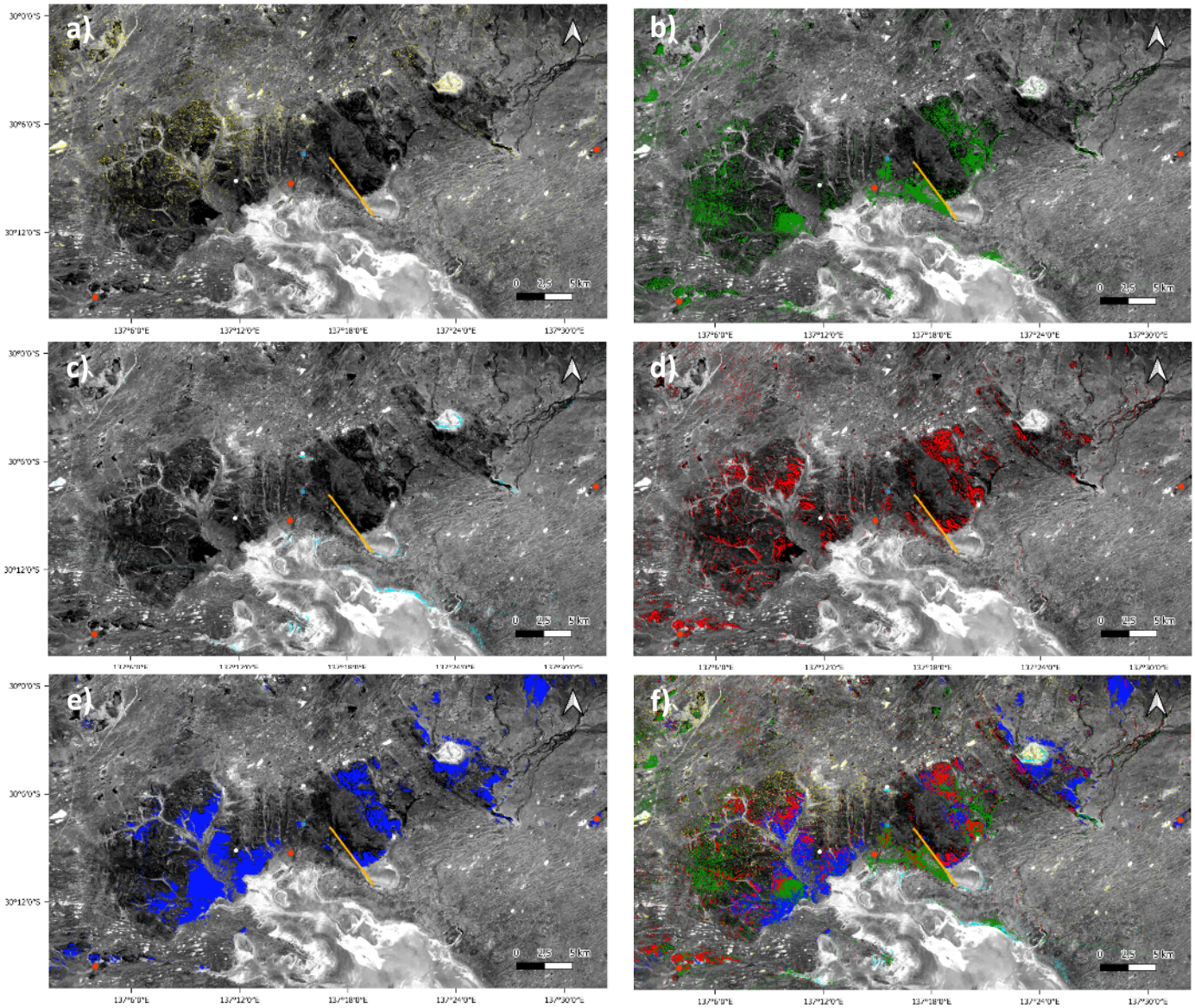

Figure 4. ASTER band ratio results in colour overlaid on Landsat B4: (a) Phyllic alteration (B5+B7)/B6, (b) Propylitic alteration (B6+B9)/(B7+B8), (c) Argillic alteration (B4+B6)/B5, (d) Fe oxide Cu-Au alteration (B5/B4), (e) Fe oxide Cu-Au alteration (B5/B4), (f) alterations exposed in the same scene. Orange dots (copper), White dots (Opal), Blue dot (Agate), gray dot (Clay) , orange line (fault). Mineral occurrences from Department for Energy and Mining(n.d)

3.1 Band ratio

Landsat image processing using band ratios also revealed valuable information about mineralization in the study area. According to Githenya, L. et al. (2019), the combination of the RGB band ratios(4/2,6/7,6/5) (Figure 3b). allowed the identification of areas with hydrothermal alteration that are identified in dark blue (Figure 3b).

The results of Aster image processing using the ratios of phyllic, argillic, propylitic, ferrous iron and iron oxide Cu and Au alteration (Figure 4). revealed a spatial distribution of these types of alteration in the study area.

Propylitic alteration is associated with alteration of feldspars, micas and amphibole, suggesting copper mineralization.

The presence of ferrous iron is due to the presence of minerals such as hematite and goethite.

Argillic alteration is characterized by the presence of clay minerals such as kaolinite, illite and montmorillonite, as well as the presence of quartz, potassium feldspars and plagioclase.

The phyllic alteration is recognized by the presence of sericite, muscovite, illite and smectite.

The Fe oxide, Cu-Au alterations is highly related to ferrous silicates.

The Aster band ratios were taken from Younes et al. (2022) and Oliver, S,et al. (2004).

3.2 Radiometric data

The results obtained (Figure 5) indicate a good correlation between the radiometry data of potassium, thorium and uranium The highest concentrations of radioactive elements (up to 4.50% K, 22 ppm eTh and more than 8 ppm eU), and the distribution of hydrothermal alteration in the study

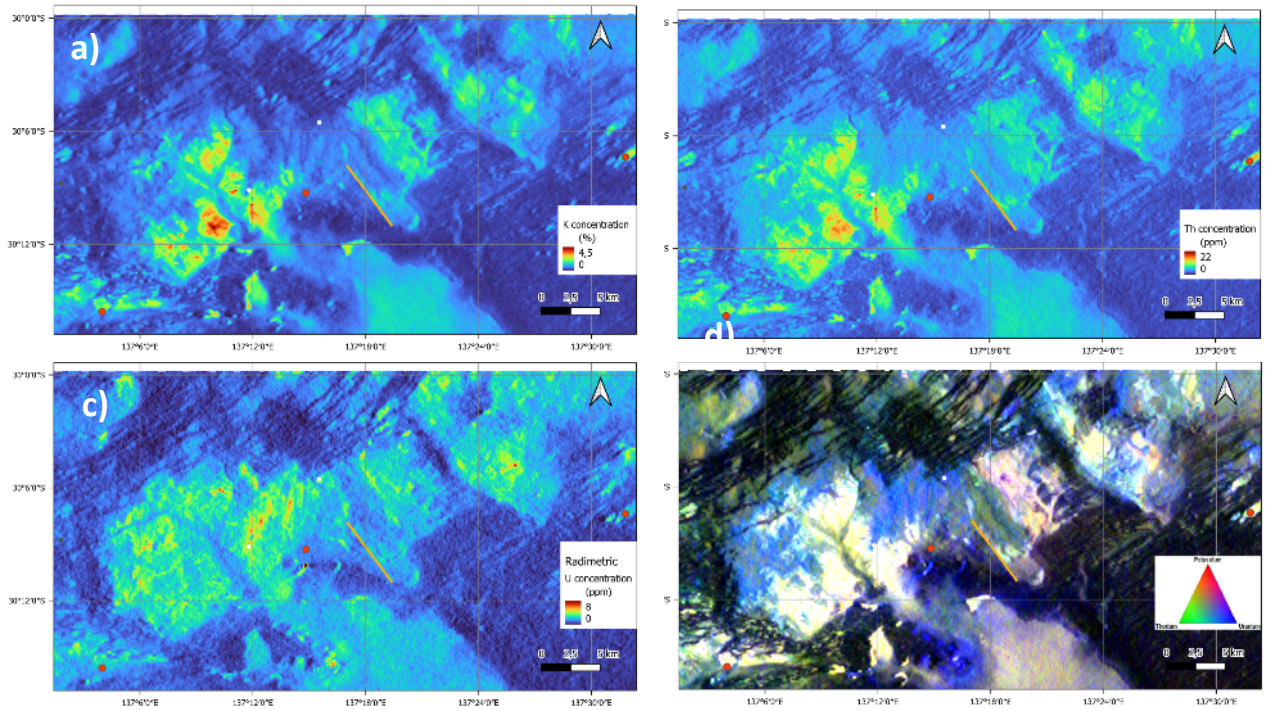

Figure 5. Maps of natural gamma-ray spectrometry : (a) Potassium (b) Thorium , (c) Uranium, (d) RGB bands (U,Th,U) Orange dots (copper), White dots (Opal), Blue dot (Agate), Gray dot (Clay) , orange line (fault). Mineral occurrences from Department for Energy and Mining(n.d)

area. Specifically, iron, copper and gold alteration was found to correlate strongly with thorium and potassium radiometry data. This suggests that these elements may be useful for the detection and exploration of mineral deposits in the area. It also reinforces the usefulness of radiometry as an important tool in mineral exploration. Uranium anomalies appear not to be associated with hydrothermal alteration zones.

4 Conclusion

hydrothermal alterations seem to be more concentrated in certain types of rocks, especially calcareous rocks. This is also because there may be more than one alteration event since some alterations are found exclusively in certain rocks.
Reported copper occurrences are mostly associated with iron, copper and gold oxide alteration, and propylitic alteration, opal is related to argillic alteration. The hydrothermal alterations are consistent with high values of thorium and potassium and can be of great help in determining alterations in other zones.

Further investigations are needed to determine more properties by means of other geophysical methods such as gravimetry and magnetometry, as well as field visits to verify the concordance of hydrothermal alterations, and to gather information associated with the IOCG type deposits in the area and the possible relationship between these and the study area.

Department for Energy and Mining, the Government of South Australia, mineral ocurrences (new versión), https://portal.geoscience.gov.au/.Accessed 2 March 2023
Geophysical Acquisition & Processing Section (2020): GSSA Andamooka percent Potassium grid geodetic. .dataset. Geoscience Australia, Canberra. http://pid.geoscience.gov.au/dataset/ga/67973
Geophysical Acquisition & Processing Section (2020): GSSA Andamooka pmm Uranium grid geodetic. .dataset. Geoscience Australia, Canberra. http://pid.geoscience.gov.au/dataset/ga/143519
Geophysical Acquisition & Processing Section (2020). GSSA Andamooka ppm Thorium grid geodetic.dataset. Geoscience Australia, Canberra. http://pid.geoscience.gov.au/dataset/ga/143523
Githenya, Lincoln & Kariuki, P. & Waswa, Aaron K.. (2019). Application of Remote Sensing in Mapping Hydrothermal Alteration Zones and Geological Structures as Areas of Economic Mineralization in Mwitika-Makongo Area, SE Kenya.
Google Maps (2023). *South Australia*, Google Maps [QGIS].https://mt1.google.com/vt/lyrs=y&x={x}&y={y}&z={z}.Accessed 07 March 2023
Oliver, S., Kalinowski, A (2004). ASTER Mineral Index Processing Manual. Geoscience Australia, Canberra.
Raymond, O.L. 2002. Scanned 250K Geological Maps. Geoscience Australia, Canberra. http://pid.geoscience.gov.au/dataset/ga/71367
Younes, Mamouch & Attou, Ahmed & Abdelhalim, Miftah & Ouchchen, Mohammed & Dadi, Bouchra & Achkouch, Lahsen & Et-Tayea, Yassine & Allaoui, Abdelhamid & Boualoul, Mustapha & Randazzo, Giovanni & Lanza, Stefania & Muzirafuti, Anselme. (2022). Mapping of Hydrothermal Alteration Zones in the Kelâat M'Gouna Region Using Airborne Gamma-Ray Spectrometry and Remote Sensing Data: Mining Implications (Eastern Anti-Atlas, Morocco). Applied Sciences. 12. 957. 10.3390/app12030957.

The use of total-field data for mineral exploration

Christopher Parker[1]
[1]*Gap Geophysics Australia Pty Ltd*

Abstract. Fast sampling magnetometers make it possible to collect total b-field data for use in mineral exploration. Total-field data is collected in Sub-Audio Magnetics (SAM) and SAMSON surveys.
The surveys can be deployed as a galvanic source to measure magnetometric conductivity (MMC) or through inductive source to measure the secondary eddy currents from conductors.
Total-field surveys are customisable and scalable depending on the requirements.
SAM surveys can be deployed on foot or in the air with a UAV or helicopter (HeliSAM). The SAM technique in galvanic mode excels at mapping electrical pathways of faults, shears, conductors.
Inductive surveys are comparable to standard electromagnetic surveys. The surveys can be undertaken as stationary measurements (SAMSON mode), walking or by air. SAMSON is the most sensitive technique and can detect large conductors that are greater than 1 km from surface. Walking or aerial surveys are known to have detected conductors in excess of 600 m below the surface.
Total-field surveys are cost effective as they allow for measurements to be taken continuously. The sensor does not suffer from rotational or vibration noise. Surveys can cover large survey areas rapidly for cost effective deep exploration.

1 Introduction

Gap Geophysics Australia Pty Ltd (GAP) developed a fast-sampling receiver that is capable of recording magnetic fields up to 9600 Hz when coupled with a Cs vapor magnetometer. The receiver samples the Larmor frequency from a compatible Cs magnetometer, such as a Geometrics G822A, very accurately. The Larmor frequency is directly proportional to the ambient magnetic field where the frequency is converted by using the gyromagnetic constant for Cs 133 which is 3.498572 Hertz per nT. Prior to this system being available, there were few other systems available that were fast enough sampling with low noise and high sensitivity. Noise levels of this system are lower than systems utilising the MFAM sensor developed by Geometrics in 2015.

2 Sub-Audio Magnetics

Sub-Audio Magnetics (SAM) (Boggs et al. 1998), was developed by Dr Malcolm Cattach as part of his PhD project in 1996. The SAM method requires a time-varying electric current to be artificially applied to the ground.

For SAM magnetometric (MMC) surveys, this is achieved with a geophysical transmitter producing a low frequency square wave (Figure 1) that is introduced into the ground through distant electrodes as for conventional gradient array electrical resistivity (ER) or induced polarisation (IP) surveys (Figure 2). SAM fixed loop electromagnetic (FLEM) surveys use a geophysical transmitter to transmit electrical current through a loop as for conventional FLEM surveys (Figure 3).

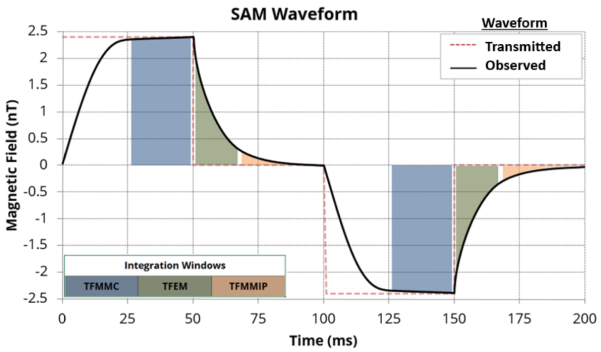

Figure 1. SAM transmitted waveform and integration windows.

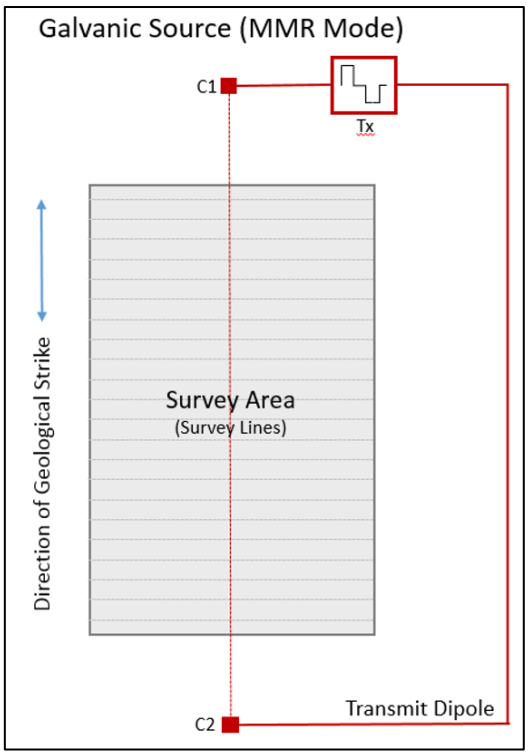

Figure 2. SAM - Galvanic mode.

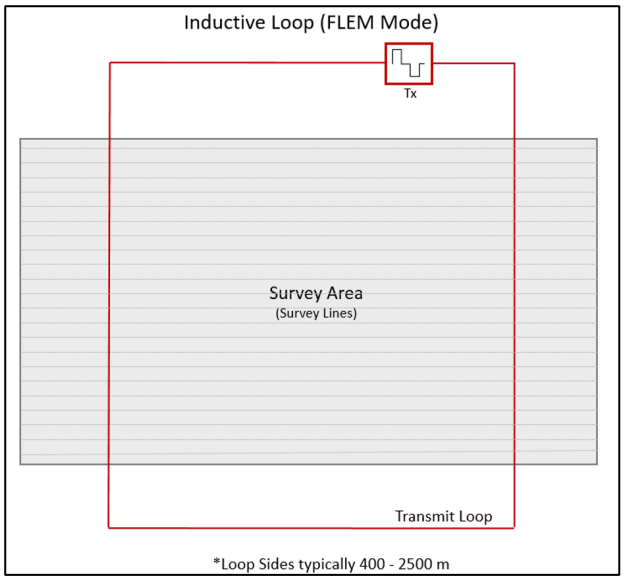

Figure 3. SAM - Inductive mode.

2.1 Galvanic mode

Galvanic mode SAM surveys are suitable for structural mapping trends, faults, shear zones and dislocations. Multiple survey orientations can be surveyed for maximum insight. Electrical pathways of least resistance or flows around resistive features are highlighted. The technique does not require highly conductive targets but rather a conductivity contrast between target geologies or structures.

2.2 Inductive mode

Fixed loop electromagnetic surveys are conducted to conducted to identify ore-bearing strata and ore-controlling structures in the mining area's periphery (Wu et al. 2022). Fixed loop surveys allow for a large magnetic moment which allows for excitation of deep targets.

3 Magnetometric Conductivity Data Recovery

SAM waveforms are separated from the spatial magnetic field and stacked to enhance the signal to-noise ratio. Raw TFMMC values are then computed by integrating beneath the waveform during the transmitter on-time. Normalisation of TFMMC values is performed by dividing by the transmitter current used. The uncorrected TFMMC values thus determined have units of picoteslas per amp (pT/A).

3.1 Primary and Normal Corrections

The theoretical electromagnetic fields produced by the wire feeding the electrodes (primary field) and current flowing through a homogenous half-space (normal field) are computed and subtracted from the raw TFMMC data. The resulting corrected TFMMC data then represent the anomalous part of the signal and the consequence of perturbations in current flow caused by lateral conductivity variations.

3.2 Magnetometric Conductivity Transformation

The TFMMC parameter is a total-field measurement that is made in the presence of the large background magnetic field of the Earth. This results in the TFMMC field being a pseudo-component measurement made in the direction of the Earth's magnetic field. As this component direction is variable from site to site and grid to grid, TFMMC data are generally non-standard and not intuitively interpreted.

The MMC transform was developed by David Boggs (Boggs et al. 1999) to provide a standard, intuitive presentation format for TFMMC data. This can be done via a 2D fast Fourier transform resulting in a horizontal component grid file. This transform is routinely applied to the gridded TFMMC data along the traverse line direction and magnetometric conductivity (MMC) images generated from these grid files.

MMC data are more readily related to underlying conductivity structure than TFMMC data. In general terms, MMC highs may be associated with underlying features that are relatively conductive and lows with resistive features.

4 Off-time Data Recovery

Total-field electromagnetic (TFEM) data are measured in the transmitter off-time. In the off-time both electromagnetic (EM) and induced polarisation (IP) responses can manifest, though the latter normally requires transmit frequencies as low as 0.125 Hz to be visible above the EM response. Due to the requirement that dynamic mode SAM uses higher frequencies, the successful extraction of IP parameters is generally restricted to resistive ground or stationary mode (SAMSON). However, EM responses can usually be detected in Total-field data and may be of significant exploration benefit. Total-field off-time data are extracted by integrating under the decay curve and involves summing the off-time data under the decay curve for each time gate and stacking readings in a moving window.

5 Platforms

Data can be collected by stationary measurements, whilst walking or flying the system with a UAV or helicopter. Highest resolution data is achieved with ground-based surveys whereas UAV and helicopter systems can be deployed in more challenging terrain or where rapid data acquisition is required.

6 Fixed loop case study – Lalor

6.1 The Lalor deposit

The Lalor deposit is a volcanogenic massive sulphide (VMS) deposit located in Manitoba, Canada. The Lalor deposit was discovered by

Hudbay Minerals using down-hole electromagnetics. The bore hole for the survey was a target from a Crone fixed-loop electromagnetics survey.
The Lalor Lake VMS deposit is flat lying, with mineralisation beginning at approximately 570 m from surface and extending to a depth of approximately 1,170 m (Blakley 2008).
Lalor deposit is geophysically characterised as a deeply buried good conductor that exhibits electrical responses that are distinct from the relatively resistive background (Yang et al. 2017).

6.2 Survey configuration

A fixed-loop electromagnetics survey was conducted over the deposit in 2014 by GAP. A total of 93 line-kilometres were acquired at 100 m line spacing in 4 hours with a towed bird receiver. The transmit loop was energised at 7.5 Hz by a Phoenix TXU-30 transmitter producing a magnetic moment of 57 MA m^2. Using this configuration, total-field was the first technique to detect the Lalor deposit with an airborne sensor.

6.3 Test lines

A test line was flown at three different transmit frequencies. The peak responses at 23 ms after the transmitter shutoff are detailed in Figure 4 with the response ranging from 3.6 pT/A at 7.5 Hz to 5.15 pT/A at 3.75 Hz.

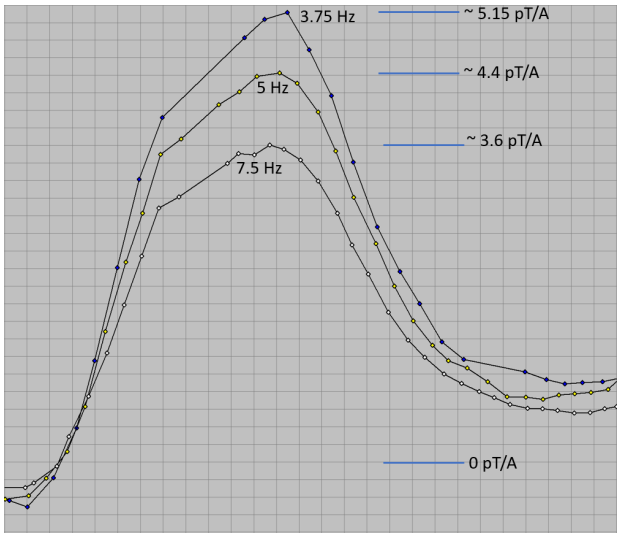

Figure 4: Peak response from the Lalor deposit.

6.4 EM response

The gridded results from channel 1, channel 9 and channel 13 are shown in Figures 5-7. The transmit loop is shown as a black outline on top of the EM response. North is up in these figures. Early time data (channel 1) is contaminated by cultural infrastructure. The response from the ore body is clear in channel 9 and channel 13.

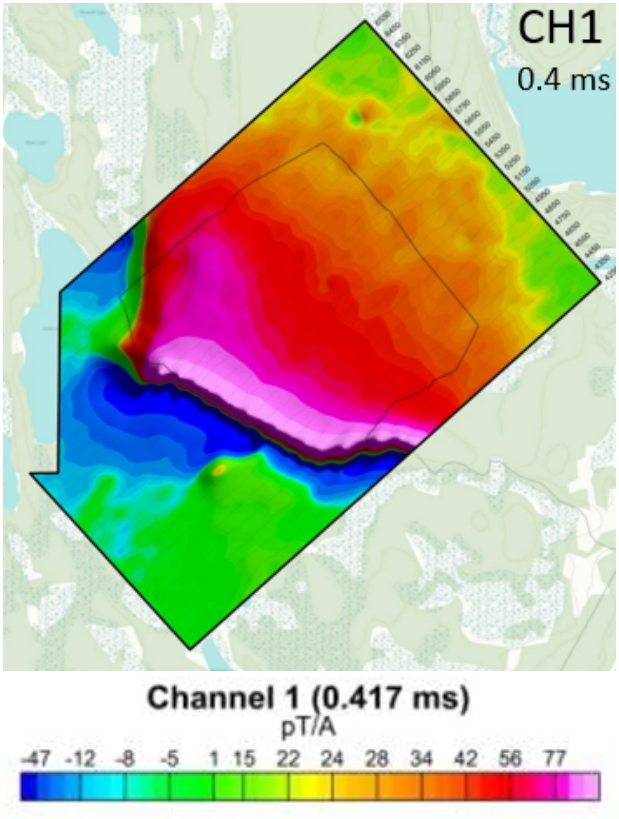

Figure 5. Lalor EM response - Channel 1.

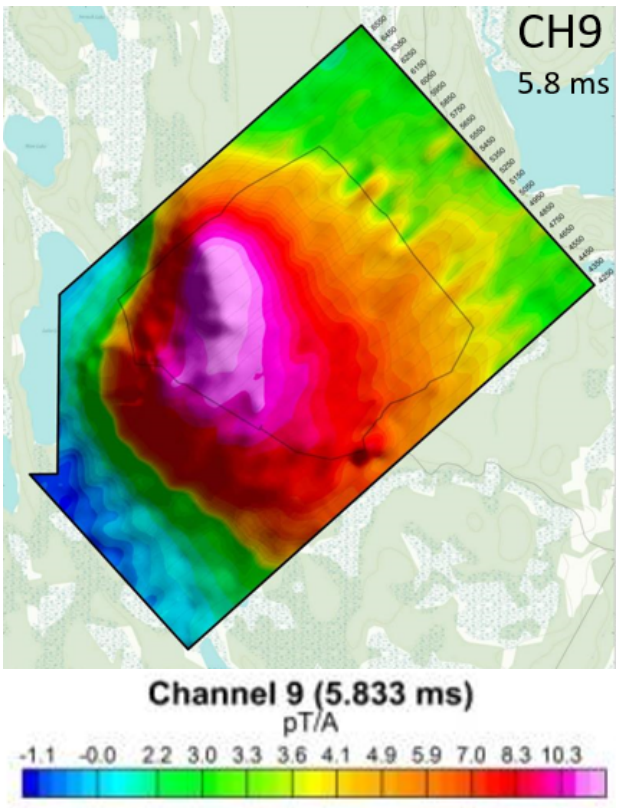

Figure 6. Lalor EM response - Channel 9.

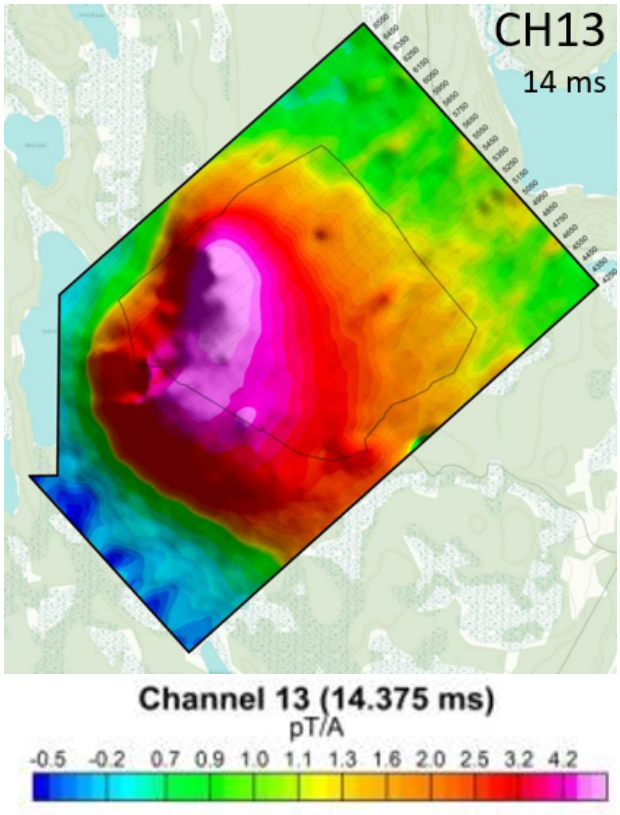

Figure 7. Lalor EM response - Channel 13.

6.5 Inversion

Inversion of the dataset was performed by Dikun Yang and Douglas W. Oldenburg. Both blind and warm-start inversions were performed. A good fit was achieved in the late time channels after the response from infrastructure was minimal.

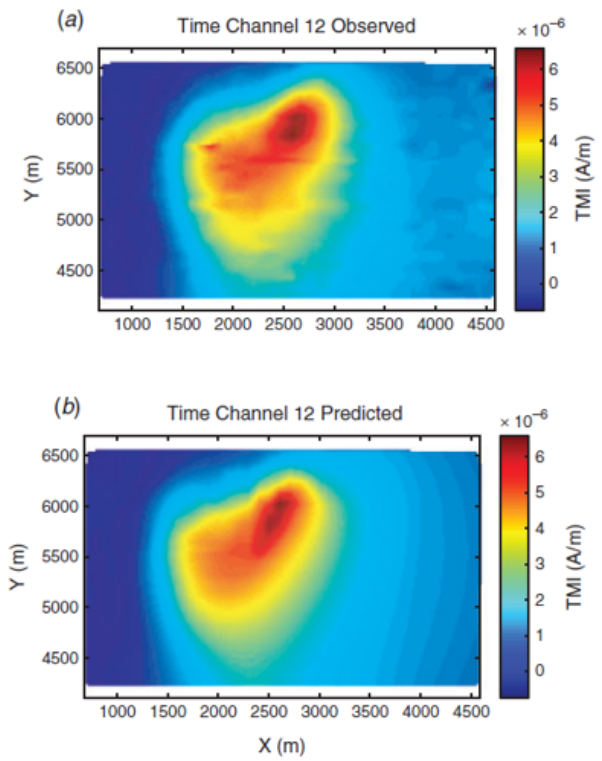

Figure 8. Lalor model Channel 12 (Yang et al. 2017)

7 Conclusion

Total-field is capable of rapid and cost-effective data collection. As the magnetometer does not require leveling or orientation, data is able to be collected from a variety of platforms resulting in an adaptable and scalable system. The Lalor deposit detection shows that the system is capable of detecting conductors at depth.

Acknowledgements

Dr Malcolm Cattach for sharing your knowledge and wisdom and for driving the development of total-field magnetometers for mineral exploration in Australia.

Dikun Yang and Douglas W. Oldenburg for inverting the HeliSAM data for the Lalor deposit.

Hudbay Minerals for allowing the HeliSAM survey to take place.

References

Blakley, I. T., 2008, Report on the Lalor Lake Deposit,SnowLake: NI 43–101 Report, Scott Wilson Roscoe Postle Associates.

D.B. Boggs, M.K. Cattach & J.M. Stanley (1998) Feasibility studies of TFMMIP and TFEM surveying with Sub-Audio Magnetics, Exploration Geophysics, 29:3-4, 290-295, https://doi.org/10.1071/EG998290

D.B. Boggs, J.M. Stanley & M.K. Cattach (1999) Three-dimensional numerical modelling of Sub-Audio Magnetic data, Exploration Geophysics, 30:3-4, 147-156, https://doi.org/10.1071/EG999147

Dikun Yang & Douglas W. Oldenburg (2017) 3D inversion of total magnetic intensity data for time-domain EM at the Lalor massive sulphide deposit, Exploration Geophysics, 48:2, 110-123, https://doi.org/10.1071/EG15070

Junjie Wu, Qingquan Zhi, Xingchun Wang, Xiaohong Deng, Yuge Liu, Xiaodong Chen, Fixed-loop TEM surveying using the SQUID magnetometer for deep mineral exploration in a conductive area, Journal of Geophysics and Engineering, Volume 19, Issue 6, December 2022, Pages 1300–1307, https://doi.org/10.1093/jge/gxac084

Smit, J.P., Stettler, E.H., Price, A.B.W. et al. Use of drones in acquiring B-field total-field electromagnetic data for mineral exploration. Miner Econ 35, 455–465 (2022). https://doi.org/10.1007/s13563-021-00292-1

Muon Tomography for Mineral Exploration and Resource Delineation

Douglas Schouten[1]
[1]Ideon Technologies, Inc., Adjunct Professor of Physics Simon Fraser University

Abstract. Muon radiography is a method of inferring average material density by measuring the attenuation of cosmic ray muons along a path length through matter. The technique is analogous to X-ray scanning in medical imaging, and similarly to computed tomography (CT) scans, muon tomography generates three-dimensional density maps from multiple muon radiographic images.

In this paper we show how muon attenuation tomography can be powerfully utilized for discovering and mapping underground mineral resources, at depths down to one kilometre underground. We will present the muon tomography method, discuss its various applications in mineral exploration and mine operations, and demonstrate its efficacy through both real-world case studies and simulations, using borehole and in-mine muon tracking detectors (also known as telescopes), in combination with other geophysical and drill data. We leverage joint inversion capabilities to yield unique, high resolution insights from disparate geoscience data, undergirded by the high resolution capability of muon tomography.

New lithostructural map of the Doropo region, northeast Côte d'Ivoire: insight from structural and aeromagnetic data

Zaindjêdé H. Siagné[1,2], Tahar Aïfa[2], Alain Nicaise Kouamelan[1], N'guessan Nestor Houssou[1], Wilfried Digbeu[1], Bi Koffi Fidèle Kakou[3], Pierrick Couderc[3]

[1]Université Félix Houphouët-Boigny, Abidjan-Cocody, 22 BP 582 Abidjan 22, Côte d'Ivoire

[2]Univ Rennes, Géosciences Rennes – CNRS UMR6118, Bat.15, Campus de Beaulieu, 35042, Rennes cedex, France

[3]Ampella-Centamin, 20 BP 945 Abidjan 20, Côte d'Ivoire

Abstract. This study, performed in the Doropo region (northeastern Côte d'Ivoire) in the Paleoproterozoic domain (southern part of the West African Craton), aims to produce a detailed lithostructural map of this area. The geology of this region is less known due to the thick lateritic overburden and the scarcity of outcrops. Recent airborne geophysical data integrated with field structural and lithological observations allowed to distinguish several lithologies. Filtering techniques (derivatives, upward continuation, etc.) showed the presence of faults, shear zones and intrusions. The structural analysis revealed four deformation events : D1 is a N-S compression marked by E-W foliation, conjugate NE-SW and NW-SE sinistral and dextral shears, respectively, as well as folds with E-W axial planes; D2 is a major transpressive phase characterized by an intense NE-SW foliation, E-W dextral shear zones, a weakly dipping stretching lineation plunging N-E, and NE-SW faults; D3 is a NE-SW compressional phase generated NW-SE foliation with ~E-W shears, and NW-SE axial plane folds; D4 is a late, rather brittle phase characterized by brittle structures (faults, fractures, etc.) and the emplacement of NE-SW and NW-SE dolerite dykes. This tectonic evolution demonstrates that the Doropo region was subject to ductile and then brittle deformations.

1 Introduction

The Paleoproterozoic terrains of the West African Craton (WAC), particularly those of the Man-Leo Shield (Figure 1), are composed of granitoid and greenstone belts. They represent an interesting target for mineral exploration because they contain numerous mineral deposits (Goldfarb et al. 2017). Unfortunately, these regions are very often characterized by surface weathering (lateritization) and limited outcrops that can hinder cartographic surveying, mineral exploration and structural studies. The recourse to use high resolution aeromagnetic data processing appears then as an essential tool to study these terrains. Magnetism has shown its effectiveness in the study of similar terrains, especially within the WAC by producing new geological data .

Thus, the recently acquired (2015) aeromagnetic data in the Doropo region (northeast Côte d'Ivoire) present an opportunity to investigate this region where no significant geological studies have been done. This region appears promising for mineral prospects, with the current presence of several exploration companies (e.g., Ampella-Centamin Co). Based on this mining interest, detailed geological studies have become a necessity, as most mineral deposits (e.g., gold) are structurally controlled (Mériaud et al. 2019; Murray et al. 2019; Tourigny et al. 2019).

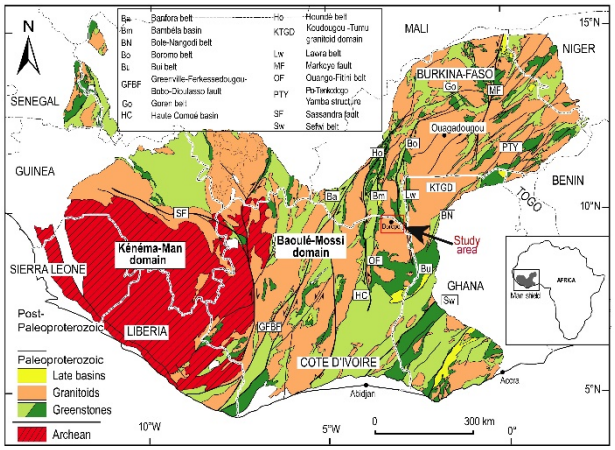

Figure 1. Simplified geological map of the Man-Leo Shield with the location of study area (modified from BRGM SIGAfrique map, Milési et al. 2004)

2 Methodology

Two major approaches (field and geophysical data analysis) were necessary to produce a detailed map of the region. A field phase was used to collect lithological, structural and magnetic susceptibility data followed by the processing of aeromagnetic data. All data acquired (geophysical, lithological and structural) were integrated within a GIS software for interpretation.

Field work resulted in: - Identifying the different lithologies encountered, describing them macroscopically. The macroscopic description focused on textural and mineralogical features. The structural framework was described by highlighting the structures that are manifestation of deformations that have affected these different lithologies while specifying their direction and dip if possible.

Above all, by establishing their spatial, crosscutting relationships and relative chronology between different deformation events. The aeromagnetic data were acquired within the framework of the Doropo Project in northeast Côte d'Ivoire. A total of 21,589 km of lines were flown. The flight lines were spaced at intervals of 200 m and 100 m (filling) in the direction N160–N340 while the control lines were spaced 2000 m and 1000 m (filling) in the direction N070–N250 at an average flight altitude of 100 m. The aeromagnetic data obtained underwent a first processing by making

specific corrections to be used and reliable for the further processing (Allard and Bois 1999).

Diurnal, altitude, topography and latitude corrections were applied. After that, the data from these corrections were gridded on a 25 m × 25 m cell size using Geosoft Oasis Montaj software. This allowed to obtain the total magnetic intensity map on which several filters were applied in order to highlight the geological properties.

3 Results

3.1 Petrography

Field observations complemented by drill core samples allowed to distinguish several lithologies in the Doropo region. The main lithologies in order of abundance are: (i) ***Biotite granite*** is the dominant lithology in the region and it is encountered all across the study area. It may occur in massive or circular or dome or slab of extremely variable size (meter to kilometer). It can also be observed as a cluster of large blocks exposed by erosion.

The rock is leucocratic to mesocratic and ranging from fine-to coarse-grained (Figure 2a). Based on visual estimation, the rock is mainly composed of quartz (~60%), feldspar (~30%), biotite (~10%) and sometimes small euhedral crystal of sulphides (ii) ***Gneissic and migmatitic granites*** are found in the south, east and north of the study area. They appear as circular or large slabs and are cross-cut by several quartzo-feldspathic veins (Figure 2b) and contain mafic enclaves (Figure 2c). They are light-to grey coloured, medium-to coarse-grained, and show a gneissic texture defined by alternating light colour (quartz, feldspar) and dark colour mineral (mica, amphibole) rich beds, which sometimes are migmatitic. Furthermore, the rocks contain quartz (~55%), feldspar (~35%), biotite (~5%), and some rare amphibole (~3%) and magnetite. (iii) ***Granodiorite*** are most often found in contact with or as enclaves within the biotite granite. They occur as circular or slab or meter-size block, and are mesocratic, medium-to coarse-grained (Figure 2d).

The rocks also show a granitic texture and contain feldspar (~60%), quartz (~25%), amphibole (~10%), biotite (~5%) and accessory sulphide minerals. These rocks sometimes show a weak foliation defined by aligned amphibole and biotite grains. (iv) ***Gabbro*** occurs in the shape of small decimeter-size nodules or as enclaves within the biotite granite and is found in the northern part of the study area. The rock is melanocratic, medium-to coarse-grained, and consists of feldspar (~70%), pyroxene (~25%), and rare amphibole (<5%) (Figure 2e). (v) ***Amphibolite*** generally occurs as enclaves within the biotite granite, gneissic and migmatitic granites, granodiorite and tonalite. The rock is dark green, fine-to medium-grained, and is crossed by numerous deformed thin quartz and feldspar veins (Figure 2f). It is mainly composed of amphibole (~80-70%) and feldspar (~30%). (vi) ***Rhyolite*** is less represented in the study area and appears as small meter-size boulders or dome-like outcrops in its central part. To the naked eye, the rock is light in colour, glassy, and composed of quartz and feldspar phenocrysts and some disseminated pyrite crystals (Figure 2g). It is the only felsic volcanic unit encountered in the Doropo region and show no apparent metamorphic alteration.

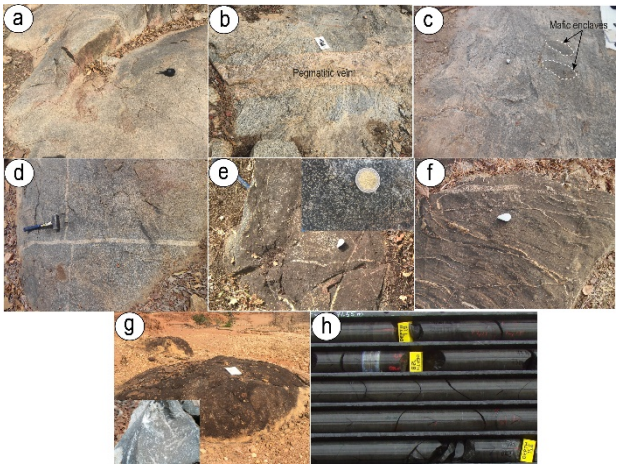

Figure 2. Field photographs of the main lithologies from the Doropo region. (**a**) Biotite granite, (**b**) Gneissic granite crossed by pegmatitic vein, (**c**) Migmatitic granite with mafic enclaves, (**d**) Outcrop of granodiorite, (**e**) Gabbro crossed by quartzofeldspathic vein, (**f**) Amphibolite with numerous thin quartz and feldspar veins, (**g**) Rhyolite boulders, and (**h**) Dolerite dyke in drill core.

3.2 Structural analysis Arial Bold 10pt

The Doropo region owes its structure to four deformation phases (D1, D2, D3 and D4) among which D1 to D3 played a major role. All of these deformation events have affected the granitoid terrains. The first deformation phase is characterized by a tectonic fabric obtained during recrystallization and migmatization (Figure 3).

This D1 deformation phase having generated: (i) a E-W S1 foliation, (ii) conjugate sinistral and dextral shear zones oriented NE-SW and NW-SE, respectively and (iii) F1 folds with plunging axis 45◦ towards the southwest. It is the result of a N–S compression which is less expressed in the region. This deformation phase has been reported in other areas of the Man-Leo Shield.

This first deformation phase (D1) is followed by a NW-SE transpressive phase (D2) which is the most important in the Doropo region (Figure 4). It is also recognized as one of the major phases at the WAC scale: (i) Northwestern and Southwestern Ghana, (ii) Northeastern Côte d'Ivoire (iii) in Burkina-Faso and (iv) in the Kédougou-Kéniéba Inlier (KKI) in Sénégal. It is distinguished by intense NE-SW oriented S2 foliations, intrafolial F2 folds, mineral stretching L2 lineations slightly sloping towards the northeast, NE-SW oriented faults (highlighted on the aeromagnetic maps) plunging, and E-W shear zone. These large-scale NE-SW oriented faults are affected by a later NNW-SSE faults. Furthermore, folding observed within granitoids could be explained by the

deformation intensity which prevailed in the Doropo region.

The D2 deformation phase is followed by two late phases: D3 and D4. D3 seems to be responsible for the shear bands, micro-folds as well as the S3 foliation present in the granitoids (Figure 5). It is related to NE-SW compression, described as late by Vidal et al. (1996) and Block et al. (2016).

The D4 deformation phase is characterized by a set of brittle structures and also the emplacement of the NE-SW and NW-SE dolerite dykes (Figure 6). These dykes may have been emplaced along the large NE-SW and NW-SE oriented faults which were reactivated during this deformation event.

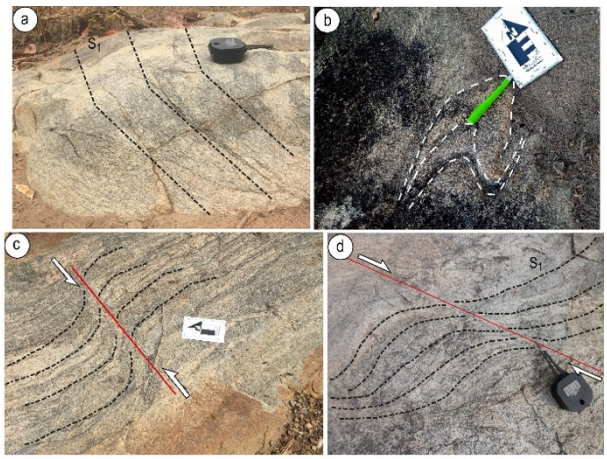

Figure 3. Structures of the D1 deformation observed in the field. **(a)** E-W Foliation (S1) in the gneissic granite of Doropo; **(b)** F1 Fold in the gneissic granite of Bouko; **(c)** NE-SW sinistral shear in the migmatitic granite of Lagbo; **(d)** NW-SE dextral shear in the gneissic granite of Doropo.

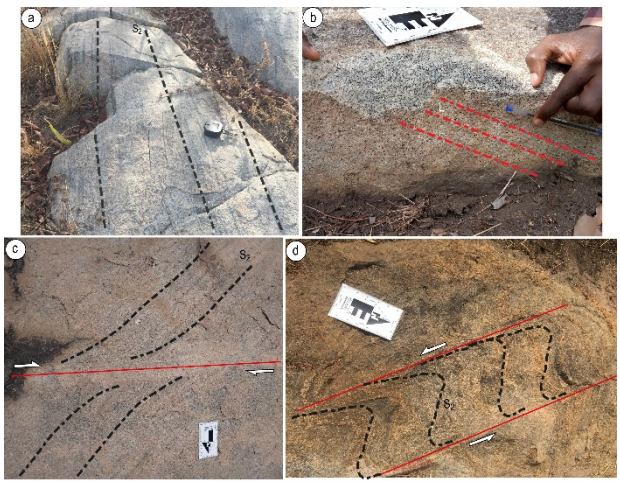

Figure 4. Representative structures of the D2 deformation. **(a)** NE-SW Foliation (S2) within the gneissic granite of Bouko; **(b)** Stretching L2 lineation within Bouko's gneissic granite; **(c)** E-W dextral shear observed at Bouko and **(d)** S-C fabrics in the Lagbo's migmatitic granite.

3.3 Aeromagnetic data and field observations integration

The particularity of these filters is to increase the contrasts between positive and negative anomalies. This allows to obtain three directional derivative maps according to X, Y and Z (Figure 7a-c). Figure 7a-c all show numerous linear and curvilinear structures strongly to weakly magnetic oriented in several directions. These different structures show NE-SW and NW-SE but also ENE-WSW to E-W preferential orientations.

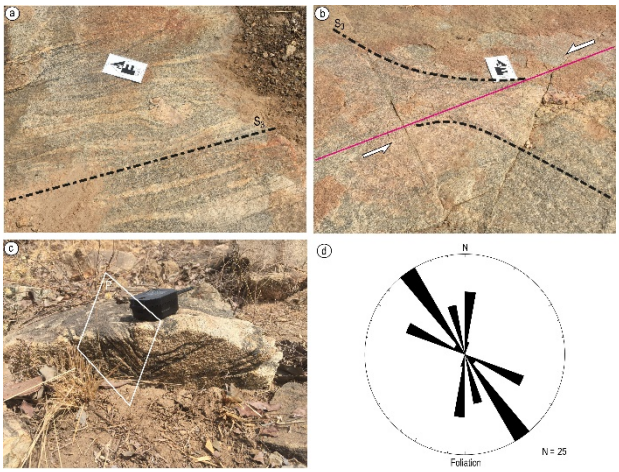

Figure 5. Structures of the D3 deformation. **(a)** NW-SE Foliation (S3) in the migmatitic granite of Lagbo; **(b)** WNW-ESE sinistral shear in Lagbo migmatitic granite; **(c)** F3 Fold with an NW-SE axial plane observed at Gbabedjou and **(d)** directional rose diagram of the S3 foliation. P denotes the axial plane of the fold.

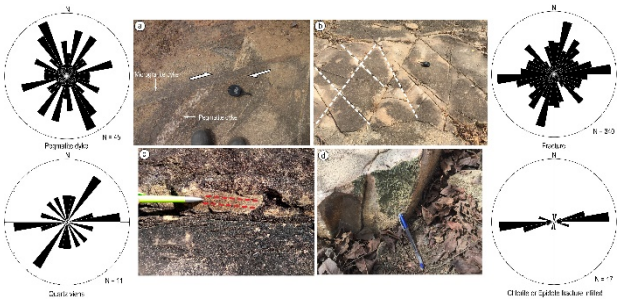

Figure 6. Structures of the D4 deformation. **(a)** Microgranite dyke dextrally shearing a pegmatite dyke; **(b)** Conjugated fractures within the Gbabedjou microgranite; **(c)** Fault mirror with subhorizontal slickenslide lineations reflecting a sinistral shear; **(d)** Fracture plan showing an infill with epidote or chlorite.

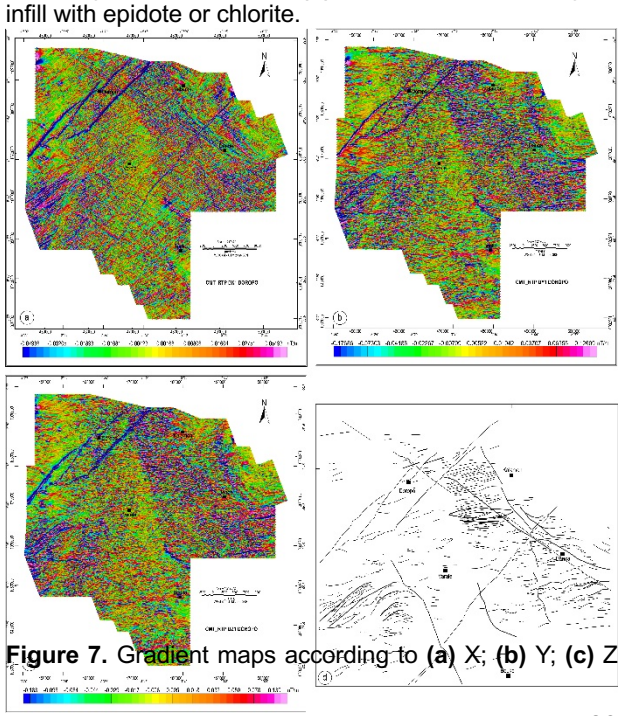

Figure 7. Gradient maps according to **(a)** X; **(b)** Y; **(c)** Z

and **(d)** Structural sketch related to faults, shears, dykes and magnetic lineaments.

The combination of geophysical data and field observations made it possible to establish the first lithostructural map of the Doropo region (Figure 8).

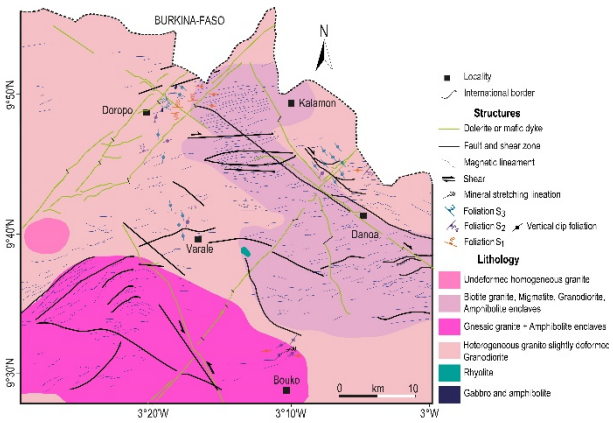

Figure 8. Lithostructural map of the Doropo region (reduction of the 1:50,000 scale map).

4 Conclusion

The geological investigations in the Doropo area have generated new lithological and structural data for the northeastern part of Côte d'Ivoire. A new interpretative lithostructural map of the region at 1:50,000 has been produced by coupling the aeromagnetic data to the field observations.

The Doropo region was deformed by four tectonic phases: (i) N-S compressional phase (D1) characterized by an E-W foliation (S1), conjugate dextral (NW-SE) and sinistral (NE-SW) shear zones, and as well as F1 folds with an E-W axial plane; (ii) most prominent NW-SE transpressional phase (D2) responsible for the regional NE-SW foliation (S2), slightly steep stretching L2 lineation plunging towards the northeast, NE-SW faults, and E-W dextral shear zones; (iii) NE-SW compressional phase (D3) marked by NW-SE foliation (S3), NW-SE axial plane F3 folds, and E-W sinistral shears, and finally (iv) late phase (D4), responsible for brittle structures (faults, fractures, etc.) and also the emplacement of NE-SW and NW-SE dolerite dykes that intersecting all the lithologies of the region.

These different deformation events suggest that the geodynamic model that has prevailed in the Doropo region was due to collisional tectonics. These new geological data are a contribution to previous studies in northeastern Côte d'Ivoire where no detailed geological study has been carried out for several decades. With the previous studies carried out in the neighboring regions of Ghana and Burkina Faso, they contribute to a better understanding of the WAC geodynamics.

Acknowledgements

We would like to thank the Managing Director of Ampella-Centamin Co. (Côte d'Ivoire) for providing us with the airborne data. This project, funded by Ampella-Centamin Co., also received funding from the West African Economic and Monetary Union (UEMOA) through its "Support Program for Training and the Research for Excellence 2019–2020 Edition".

References

Allard, M. and Bois, D. (1999): La géophysique appliquée à l'exploration minérale. Dans la magnétométrie et la radiométrie. *Centre collégial de développement de matériel didactique* (CCDM), Montréal (Québec), pp. 161–311.

Block, S., Jessell, M., Ailleres, L., Baratoux, L., Bruguier, O., Zeh, A., Bosch, D., Caby, R., Mensah, E. (2016): Lower crust exhumation during Paleoproterozoic (Eburnean) orogeny, NW Ghana, West African Craton: interplay of coeval contractional deformation and extensional gravitational collapse. Precambrian Res. 274, 82–109.

Goldfarb, R.J., André-Mayer, A.-S., Jowitt, S.M., Mudd, G.M. (2017): West Africa: the world's premier paleoproterozoic gold province. Econ. Geol. 112 (1), 123–143.

Mériaud, N., Masurel, Q., Thébaud, N., Tourigny, G. (2019): Fluid Pressure Dominated Orogenic Gold Mineralization under Low Differential Stress: Case of the Yaouré Gold Camp, Côte d'Ivoire, West Africa. Mineralium Deposita, pp. 1-18.

Milési, J.P., Feybesse, J.L., Pinna, P., Deschamps, Y., Kampunzu, H., Muhongo, S., Lescuyer, J.L., Le Goff, E., Delor, C., Billa, M., Ralay, F., Heinry, C. (2004): Geological map of Africa 1: 10,000,000, SIGAfrique project. In *20th conference of African geology, BRGM, Orléans,* France.

Murray, S., Torvela, T., Bills, H. (2019): A geostatistical approach to analyzing gold distribution controlled by large-scale fault systems-an example from Côte d'Ivoire. J. Afr. Earth Sci. 151, 351-370.

Tourigny, G., Tranos, M.D., Masurel, Q., Kreuzer, O., Brammer, S., Owusu-Ansah, K., Yao, D., Hayford, T. (2019): Structural controls on granitoid-hosted gold mineralization and paleostress history of the Edikan gold deposits, Kumasi Basin, southwestern Ghana. Miner. Deposita 54, 1033-1052.

Vidal, M., Delor, C., Pouclet, A., Simeon, Y., Alric, G. (1996): Evolution geodynamique de l'Afrique de l'Ouest entre 2.2 Ga et 2 Ga: Le style archéen des ceintures vertes et des ensembles s´edimentaires birimiens du nord-est de la Côte d'Ivoire. Bull. Soc. Geol. Fr. 167, 307-319.